Article

Nerve-to-cancer transfer of mitochondria during cancer metastasis

https://doi.org/10.1038/s41586-025-09176-8

Received: 15 April 2024

Accepted: 20 May 2025

Published online: 25 June 2025

Open access

Check for updates

Gregory Hoover[1,2], Shila Gilbert[1,2], Olivia Curley[1,2], Clémence Obellianne[3], Mike T. Lin[4], William Hixson[1,2], Terry W. Pierce[2], Joel F. Andrews[1,2], Mikhail F. Alexeyev[4], Yi Ding[5], Ping Bu[5], Fariba Behbod[6], Daniel Medina[7], Jeffrey T. Chang[8], Gustavo Ayala[5] ✉ & Simon Grelet[1,2] ✉

The nervous system has a pivotal role in cancer biology, and pathological investigations have linked intratumoural nerve density to metastasis[1]. However, the precise impact of cancer-associated neurons and the communication channels at the nerve–cancer interface remain poorly understood. Previous cancer denervation models in rodents and humans have highlighted robust cancer dependency on nerves, but the underlying mechanisms that drive nerve-mediated cancer aggressivity remain unknown[2,3]. Here we show that cancer-associated neurons enhance cancer metabolic plasticity by transferring mitochondria to cancer cells. Breast cancer denervation and nerve–cancer coculture models confirmed that neurons significantly improve tumour energetics. Neurons cocultured with cancer cells undergo metabolic reprogramming, resulting in increased mitochondrial mass and subsequent transfer of mitochondria to adjacent cancer cells. To precisely track the fate of recipient cells, we developed MitoTRACER, a reporter of cell-to-cell mitochondrial transfer that permanently labels recipient cancer cells and their progeny. Lineage tracing and fate mapping of cancer cells acquiring neuronal mitochondria in primary tumours revealed their selective enrichment at metastatic sites following dissemination. Collectively, our data highlight the enhanced metastatic capabilities of cancer cells that receive mitochondria from neurons in primary tumours, shedding new light on how the nervous system supports cancer metabolism and metastatic dissemination.

Cancer plasticity has a pivotal role in cancer heterogeneity and the emergence of adaptive phenotypes[4]. Although cancer cells often rely on glycolysis for energy, numerous studies indicate that they adapt their metabolism, including oxidative phosphorylation (OXPHOS), to changing environments. The metabolic plasticity of cancer cells is becoming increasingly recognized as essential for cancer progression by enabling cancer cells to efficiently navigate through the metastatic cascade[5,6]. Studies on cancer metabolic plasticity have primarily focused on cell-autonomous mechanisms, in which cells modify their metabolic program and perform metabolic rewiring by regulating metabolic enzymes and adapting alternative substrates. The non-autonomous mechanisms of metabolic plasticity are less well understood and can involve complex interactions within the cancer microenvironment[7]. For instance, stromal cells, including fibroblasts and immune cells, can share a variety of metabolites, growth factors and cytokines, contributing to the metabolic reprogramming of cancer[8]. Overall, non-cell-autonomous mechanisms of the cancer cells' metabolic plasticity are still unclear and may represent promising targets for preventing metastatic dissemination.

Many cancers are innervated, and in recent years, cancer neurobiology has garnered considerable attention[1]. Studies scrutinizing the impact of the nervous system in various cancers have established a critical role of cancer-infiltrating neurons in controlling cancer aggressivity, including supporting cancer cell metabolism through direct metabolic interactions[1,9]. Pathological analyses in patients with cancer consistently associated cancer innervation with negative clinical outcomes, and targeted ablation of intratumoural nerves can suppress cancer growth in a tissue-specific manner[1,10–12]. The neuronal component of the cancer microenvironment can arise from the recruitment of pre-existing nerves through perineural invasion or the de novo generation of nerves within the cancer stroma through cancer neurogenesis[13,14]. Nerve withdrawal in human prostate cancer demonstrated impaired tumour growth and metabolism, and metabolomic analysis of denervated cancers across rodent and human species revealed disrupted metabolic efficiency that is characterized by their downregulated mitochondrial metabolism and transition of the cancer cells into a more glycolysis-dependent production of energy[2]. Overall, converging evidence indicates that denervated cancer actively suffers from nerve withdrawal, with a predominant effect on their energetic metabolism[1,15].

[1]Department of Biochemistry and Molecular Biology, Frederick P. Whiddon College of Medicine, University of South Alabama, Mobile, AL, USA. [2]Mitchell Cancer Institute, University of South Alabama, Mobile, AL, USA. [3]Department of Microbiology and Immunology, Frederick P. Whiddon College of Medicine, University of South Alabama, Mobile, AL, USA. [4]Department of Physiology and Cell Biology, Frederick P. Whiddon College of Medicine, University of South Alabama, Mobile, AL, USA. [5]Department of Pathology and Laboratory Medicine, University of Texas Health Science Center at Houston, McGovern School of Medicine, Houston, TX, USA. [6]Department of Pathology and Laboratory Medicine, University of Kansas Medical Center, Kansas City, KS, USA. [7]Department of Molecular and Cellular Biology, Baylor College of Medicine, Houston, TX, USA. [8]Department of Integrative Biology & Pharmacology, University of Texas Health Science Center at Houston, Houston, TX, USA. ✉e-mail: gustavo.e.ayala@uth.tmc.edu; sgrelet@southalabama.edu

These studies demonstrated the cancer metabolic dependency on nerves and suggested the existence of metabolic support mechanisms acting at the nerve–cancer interface. However, their nature remains unknown, and characterizing these mechanisms, which represent a critical gap in the understanding of the metabolic support provided by nerves to cancer cells, is the focus of this study.

Here we demonstrate the metabolic dependency of breast cancer cells on nerves. Using orthogonal in vitro and in vivo methods, we observed the prevalence of transfers of mitochondria between neurons and cancer cells. To trace the fate of the recipient cells, we developed MitoTRACER, a genetic reporter that permanently marks cancer cells receiving mitochondria from donor cells. Our approach revealed that neuron-derived mitochondria enhance cancer cell metabolic capacity, stemness and resistance to metastatic stressors. Fate mapping of the recipient cells in vivo has shown their increased metastatic capacities. In the human context, multispectral imaging with machine-learning deconvolution showed increased mitochondrial mass in metastatic cells, and perineural invasion was associated with higher mitochondrial content in cancer cells near nerves. Finally, cancer chemically denervated with botulinum neurotoxin type A (BoNT/A) confirmed reduced mitochondrial load in cancer cells. These findings highlight nerve-driven metabolic support as essential to cancer metabolic plasticity and metastatic potential.

Nerve withdrawal impairs tumour bioenergetics

Previous studies on the effects of BoNT/A-mediated prostate denervation conducted in humans and rats uncovered the cancer dependency on nerves and the metabolic reprogramming of prostate cancer cells after nerve withdrawal[2]. Similarly, breast cancer denervation resulted in a marked decrease in cancer growth[15]. However, the impact of cancer-infiltrating nerves in breast cancer metabolism has not been explored. We investigated the consequences of nerve withdrawal in breast cancer using two complementary mouse models. We first adapted a BoNT/A-mediated denervation protocol to the 4T1 model of triple-negative breast cancer (TNBC; Fig. 1a,b) and to a human ductal carcinoma in situ xenograft model[16] (Extended Data Fig. 1a–d). In both settings, transcriptomic profiling of cancer cells from control and denervated tumours revealed distinct expression signatures following denervation (Fig. 1b and Extended Data Fig. 1a,b), and Gene Ontology analyses have underscored the prevalent downregulation of metabolic processes (Extended Data Fig. 1b–d and Supplementary Tables 1–3). Gene set enrichment analysis of the ductal carcinoma in situ model identified the tricarboxylic acid cycle as the most suppressed pathway overall (Extended Data Fig. 1c and Supplementary Table 2). Histopathological examination of this model has shown a reduction in the incidence of invasive lesions from 55% in control mice to 12% in denervated mice (Extended Data Fig. 1e), underscoring the functional importance of innervation for breast cancer progression.

Cancer boosts neuronal mitochondria

To explore in more detail the mechanisms associated with cancer metabolic dependencies on nerves in breast cancer progression, we developed an in vitro nerve–cancer coculture. We mixed the 4T1 aggressive mouse breast carcinoma cells with neuronal stem cells (NSCs) from the mouse subventricular zone (SVZ) (Extended Data Fig. 2a–d), as they have been proved to be a source of cancer innervation[14]. After stimulation by 4T1 cancer cells, SVZ-NSCs rapidly undergo differentiation, evidenced by their morphological transition from round, neural progenitor cells to more elongated cells with neurite extensions and forming close contact with the cancer cell (Fig. 1c and Extended Data Fig. 2e). SVZ-NSCs can differentiate into neurons, astrocytes or oligodendrocyte glial cells. Using our coculture model, we confirmed the neuronal commitment of NSCs, as shown by microscopy through the expression of the neuronal marker tubulin β3 (TUBB3) (Extended Data Fig. 2f). Absolute quantification by flow cytometry showed that more than 90% of progenitor cells differentiated into $TUBB3^+$ and $MAP2^+$ neurons but remained negative for the glial cell markers O4 and ALDH1L1 (Extended Data Fig. 2g–i). SVZ-NSCs also exhibited neuronal functional characteristics, including calcium pulsatile activity (Extended Data Fig. 2j and Supplementary Video 2) and the ability to generate action potentials in response to depolarizing current injection, with an action potential threshold averaging −46 mV ± 5 mV as observed through whole-cell electrophysiology recordings (Extended Data Fig. 2k,l).

After establishing the biological relevance of the nerve–cancer coculture in vitro, we next confirmed that the cancer's metabolic dependency on nerves, observed in mouse xenografts, could also be replicated in a more simplistic in vitro model. Cancer cells in monoculture or cultivated in the presence of neurons were isolated before their metabolic analysis. In comparison to those cultivated alone, the cancer cells isolated from the nerve–cancer coculture exhibited upregulated mitochondrial respiration (Fig. 1d), characterized by significant increases in their basal and maximal mitochondrial respiration as well as enhanced spare respiratory capacities (Extended Data Fig. 3a). This reflects the establishment of the nerve–cancer metabolic dependencies in the coculture model in vitro.

As previously described, cancer-induced neuronal progenitor differentiation is integral to the nerve–cancer cross-talk established during cancer innervation[1]. For instance, we and others have previously demonstrated how the cancer-driven expression of axon guidance molecules such as semaphorin 4F controls the cancer-induced neuronal precursor differentiation into the cancer stroma and increases intratumoural nerve density and cancer aggressivity[17–19]. Physiologically, differentiating neuronal progenitors must undergo a metabolic shift to increase their mitochondrial metabolism and meet their specific energetic demands during physiological differentiation[20] (Extended Data Fig. 3b,c). We examined whether similar reprogramming also occurs during cancer-driven neuronal differentiation and confirmed a robust increase in the mitochondrial mass of SVZ-NSCs exposed to 4T1 cancer cells (Extended Data Fig. 3d), with absolute quantification of mitochondrial DNA (mtDNA) showing an increasing mtDNA load from about 16 to 226 mtDNA/nuclear DNA copies per neuron after their cancer-induced differentiation (Extended Data Fig. 3e). Finally, genetic fluorescent labelling of SVZ-NSC mitochondria confirmed morphological changes of the SVZ-NSCs exposed to the cancer cells and the development of an extended mitochondrial network across the nerve–cancer coculture, transitioning from globular structures in NSC monoculture to thin and elongated tubular structures extending throughout the NSCs in coculture with breast cancer cells (Extended Data Fig. 3f). Such changes represent typical hallmarks of metabolic reprogramming, in which maturing neurons transition from glycolytic to mitochondrial oxidative metabolism[20,21].

Neuron-to-cancer mitochondria transfer

The establishment of close nerve–cancer cross-talk in our in vitro cocultures, the significant increase in neuronal mitochondria abundance and the enhancement of mitochondrial metabolism in isolated cancer cells following exposure to neuronal cells in coculture suggested that metabolism-related collaboration mechanisms initiated at the nerve–cancer interface. The cell–cell transfer of mitochondria has recently become a subject of investigation as it has crucial functions in health and disease[22–24], and was recently shown to have profound effects on cancer progression[25,26]. Moreover, research has demonstrated that astrocytes can provide metabolic support to glioblastoma cells by mitochondria transfer in the central nervous system[27].

We therefore investigated whether mitochondrial transfer could occur within the peripheral nervous system and assessed whether breast cancer cells exposed to neurons could acquire neuron-derived

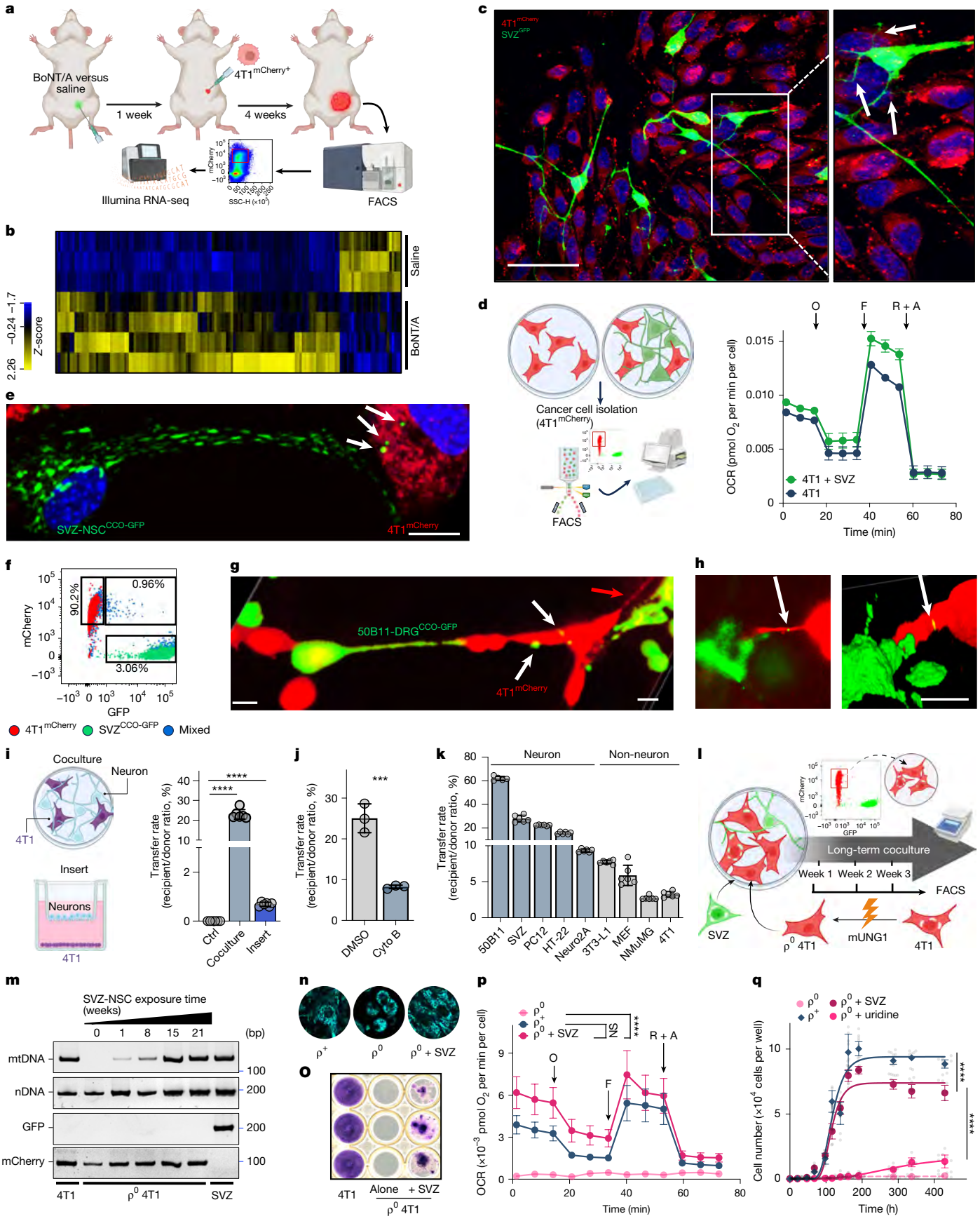

Fig. 1 | See next page for caption.

Fig. 1 | Cancer metabolic dependency on nerves and intercellular transfer of functional mitochondria at the nerve–cancer interface. a,**b**, Pre-denervation breast cancer model using BoNT/A injections in BALB/c mice followed by implantation of 4T1^{mCherry} cells. Transcriptomic analysis of 4T1^{mCherry} cells revealed a distinct transcriptomic signature and downregulation of metabolic processes. SSC-H, side scatter height; RNA-seq, RNA sequencing. **c**, Confocal micrograph of SVZ-NSCs^{GFP} mixed with 4T1^{mCherry} cells. White arrows show the establishment of neuron–cancer contacts. Scale bar, 50 µm. **d**, 4T1 cells FACS-isolated from coculture (left) showed increased OXPHOS capacities (Seahorse assay; mean ± s.e.m; representative profile (n = 3); right). O, oligomycin; F, carbonyl cyanide-p-trifluoromethoxyphenylhydrazone; R + A, rotenone and antimycin A; OCR, oxygen consumption rate. **e**,**f**, Time-lapse confocal microscopy (**e**) and flow cytometry (**f**) highlighted mitochondrial transfer from SVZ-NSCs$^{CCO\text{-}GFP}$ to 4T1^{mCherry} cells (n = 6 independent cocultures). Scale bar, 10 µm. The white arrows show transferred mitochondria. **g**,**h**, 3D reconstruction shows transfer through tunnelling nanotubes between peripheral nervous system-derived 50B11-DRG$^{CCO\text{-}GFP}$ cells and 4T1^{mCherry} cells. Red arrow shows the tunnelling nanotube structure, and white arrows show transferred mitochondria. Scale bars, 20 µm. **i**, Quantification of direct cell–cell contact (23.04%) versus distant (0.59%) transfers using Transwell inserts. Normalized transfer rate is calculated as the percentage of 4T1$^{mCherry+/GFP+}$ cells among the eGFP$^+$ cells in the coculture. Mean ± s.d., Student's two-tailed unpaired t-test; ****P < 0.0001 (n = 6 independent cocultures). Ctrl, control. **j**, Cytochalasin B (Cyto B) reduces mitochondrial transfer. DMSO, dimethylsulfoxide. Mean ± s.d., Student's two-tailed unpaired t-test, ***P = 0.001 (n = 3 independent cocultures). **k**, Mitochondrial transfer rates vary with donor cells from different origins. MEF, mouse embryonic fibroblast. Mean ± s.d. (n = 5 independent cocultures). **l**, 4T1^{mCherry} cells rendered devoid of mtDNA (ρ^0) were cocultured with ρ^+ SVZ-NSCs^{GFP} and isolated by FACS at various times to monitor the transfers. mUNG1, Y147A mutant of uracil-N-glycosylase. **m**, PCR of mtDNA content in FACS-sorted ρ^0 4T1^{mCherry} cells showed progressive reacquisition of mtDNA. Expression of GFP and mCherry confirmed the purity of the 4T1 cells. Nuclear DNA (nDNA) was used as the loading control. **n**, MitoTracker microscopy imaging of ρ^+ 4T1, ρ^0 4T1 and ρ^0 4T1 cells FACS-sorted from coculture shows rescue in their mitochondrial morphology. **o**, Reacquisition of SVZ-derived mtDNA in ρ^0 4T1 cells restores uridine-independent growth. **p**,**q**, FACS-isolated ρ^0 4T1 cells rescued by mitochondrial transfer regained OXPHOS (**p**; Seahorse assay, mean ± s.e.m.; representative profile (n = 3)) and proliferative capacities (**q**; direct cell counting, mean ± s.d., n = 6 independent cultures); two-way analysis of variance (ANOVA), ****P < 0.0001; NS, not significant. **a**, Created in BioRender. S. Grelet (2025) https://biorender.com/0j8zovf. **d**, Created in BioRender. S. Grelet (2025) https://biorender.com/oxxilqq. **i**, Created in BioRender. S. Grelet (2025) https://biorender.com/8tdz09x. **l**, Created in BioRender. S. Grelet (2025) https://biorender.com/pm5yh64.

mitochondria. To test this hypothesis, we established nerve–cancer cocultures by combining central nervous system-derived neurons (SVZ-NSCs) or dorsal root ganglia-derived neurons (50B11-DRG) with 4T1 breast cancer cells expressing the mCherry fluorophore (4T1$^{mCherry+}$). Neurons were genetically modified to express enhanced green fluorescent protein (eGFP)-labelled mitochondria (SVZ-NSC$^{CCO\text{-}GFP}$ and 50B11-DRG$^{CCO\text{-}GFP}$) (Fig. 1e–h and Supplementary Video 1). Confocal microscopy and flow cytometry analysis of the coculture confirmed mitochondrial transfer from neurons to cancer cells (Fig. 1e–h and Extended Data Fig. 4a) and the formation of tunnelling nanotube-like structures, facilitating organelle transfer (Fig. 1g, red arrow), as confirmed by three-dimensional (3D) reconstruction (Fig. 1h, white arrows). Flow cytometry (Fig. 1f and Extended Data Fig. 4a) showed acquisition of a double-positive 4T1$^{GFP+/mCherry+}$ subpopulation of cells in the cocultures that reflects the acquisition of eGFP-labelled mitochondria into the recipient 4T1$^{mCherry+}$ cells. Although this population accounts for an average of 0.96% of the total cells in the coculture (Fig. 1f), it represents only a snapshot of the current mitochondria transfers, and the SVZ-NSCs providing the mitochondria represent, on average, only 3.06% of the coculture. When normalized to the population of eGFP-labelled cells in the coculture, the double-positive (4T1$^{mCherry+/GFP+}$) fraction accounted for an equivalent of 31.4% of the donor population. This normalization method was used to standardize the transfer rate from donor to recipient cells for different experimental conditions. Beyond the direct cell–cell contact-mediated transfer of mitochondria, we investigated whether distant mechanisms, such as microvesicles, could be involved. Distant coculture using Transwell inserts confirmed that cell–cell contact is the primary route of mitochondrial transfer, although distant transfers also occurred (Fig. 1i). Inhibition of tunnelling nanotube formation further validated the role of these structures in the transfer process without a significant impact on cell viability (Fig. 1j and Extended Data Fig. 4b), as previously shown[27]. Using different cell lines, we next tested the capacities of cells with diverse origins (50B11-DRG neurons, SVZ neurons, PC12 pheochromocytoma, HT-22 hippocampal, Neuro2A neuroblastoma, 3T3-L1 pre-adipocytes, mouse embryonic fibroblasts, NMuMG normal mouse mammary gland and 4T1 breast cancer cells) in transferring their mitochondria to cancer cells (Fig. 1k). Every tested donor significantly transferred mitochondria to the recipient 4T1 cells. Notably, cell lines of neuronal origin exhibited higher mitochondrial transfer rates. In addition, we confirmed mitochondria transfer in nerve–cancer cocultures using human cancer cell lines (Extended Data Fig. 4c).

Transferred mitochondria are functional

We subsequently validated the transfer of neuronal mitochondria to cancer cells through an additional orthogonal validation approach. We generated rho-zero (ρ^0) 4T1 cancer cells lacking mtDNA and cocultured them with rho-plus (ρ^+) SVZ-NSCs[28] (Fig. 1l). PCR amplification of mtDNA from the ρ^0 4T1^{mCherry} cells confirmed a complete loss of mtDNA and revealed their gradual reacquisition of mtDNA through coculture with SVZ-NSCs (Fig. 1m and Extended Data Fig. 4d). The mitochondrial morphology was altered in ρ^0 cells, with the mitochondria exhibiting a globular and fragmented appearance as described previously[29]. This morphology was restored following the mtDNA restoration through nerve–cancer coculture (Fig. 1n). ρ^0 cells are also phenotypically characterized by the complete loss of OXPHOS capacities and auxotrophy for uridine[30,31]. Therefore, ρ^0 cells require uridine complementation to grow in culture in vitro. We tested whether transferred mitochondria are functional in recipient cells. We grew ρ^0 4T1 cells in the presence of uridine either alone or in coculture with ρ^+ SVZ-NSCs. After 5 days of coculture, 4T1$^{mCherry+}$ cells were sorted by fluorescence-activated cell sorting (FACS) and subcultured without uridine. In the absence of uridine, ρ^0 4T1 cells did not form colonies, but a subset of the ρ^0 4T1 cells enriched from coculture with ρ^+ neurons formed viable colonies (Fig. 1o), reflecting rescue of uridine synthesis, therefore demonstrating the functionality of the transferred mitochondria. The SVZ-NSC-derived mitochondria transferred to the ρ^0 4T1 cells also rescued their mitochondrial respiration and proliferative capacities as observed by Seahorse extracellular flux metabolic analysis (Fig. 1p, ρ^0 + SVZ) and proliferation assays, respectively (Fig. 1q, ρ^0 + SVZ).

Transfers are prevalent in vivo

We next tested the occurrence of nerve–cancer transfers of mitochondria in vivo. Clinically, human prostate cancer samples showed an increased mitochondrial load in cancer cells associated with perineural invasion (Fig. 2a). High-throughput multispectral imaging quantification based on machine learning[32] highlighted that cancer cells closer to nerves had a significantly higher mitochondrial load than cells farther from nerves (Fig. 2b and Supplementary Tables 4 and 5). To assess whether this increased mitochondrial load may result from mitochondrial transfer, we analysed prostate tissue from a clinical trial (NCT01520441), in which human prostate cancer was chemically denervated. Multispectral imaging revealed that cancer cells of the

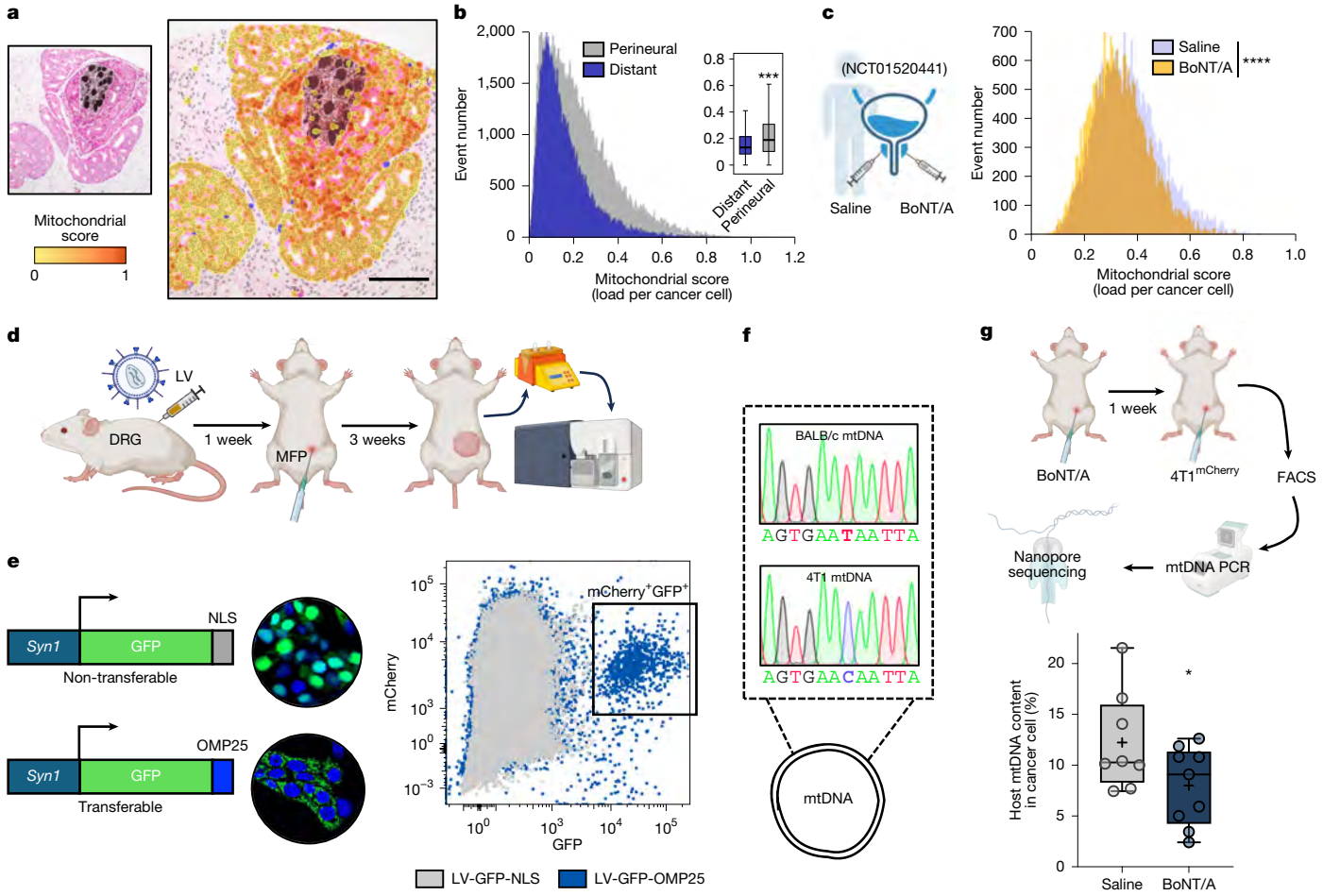

Fig. 2 | Intercellular transfer of mitochondria between host neuron and cancer. a, Histopathology of human prostate cancer with perineural invasion shows increased mitochondrial content near nerves (mitochondria are visualized by periodic acid–Schiff staining (magenta); nerves are visualized by diaminobenzidine staining (brown)). Representative profile ($n = 72$ patients). Scale bar, 180 µm. **b**, Multispectral imaging combined with machine learning-based image deconvolution, spatial correlation, and quantification indicate significantly higher mitochondrial loads in prostate cancer cells near nerves (perineural; $n = 72,40,007$ cells) compared to distant cancer cells (distant; $n = 58,20,766$ cells). The line shows the median, the box boundaries show the 25th and 75th percentiles, and the whiskers show the minimum and maximum values. Two-sided Welch's *t*-test, $^{***}P < 0.001$. **c**, BoNT/A-mediated denervation reduces mitochondrial load in human prostate cancer cells (paired analysis: saline versus BoNT/A; saline: $n = 10,918$ cells, BoNT/A: $n = 14,186$ cells). Two-sided Welch's *t*-test, $^{****}P = 1.463 \times 10^{-113}$. Clinical trial (NCT01520441). **d**, Mouse DRG neurons innervating the mammary gland were labelled with lentivirus (LV) to tag neuronal mitochondria before injection of $4T1^{mCherry}$ cells into mammary fat pads (MFPs). Cancer cells were isolated post-tumour growth for mitochondrial transfer analysis to detect host-derived mitochondrial transfer. **e**, Neuronal mitochondria were labelled using lentiviruses expressing either nuclear-localized (GFP-NLS, non-transferable) or mitochondria-localized (GFP-OMP25, transferable) eGFP under the synaptin1 (*Syn1*) promoter. Flow cytometry of cancer cells identified $eGFP^+$ subpopulations, indicating neuronal mitochondrial transfer between mouse host neurons and cancer xenografts. **f**, Sanger sequencing enabled the detection of mtDNA polymorphisms between host BALB/c cell and 4T1 cancer cell mtDNA. **g**, Oxford Nanopore sequencing analysis of mtDNA heteroplasmy in FACS-isolated cancer cells demonstrated host-to-cancer mitochondrial transfer. BoNT/A-mediated pre-denervation at the xenograft site significantly reduced mitochondrial transfer to cancer cells (saline $n = 8$, BoNT/A $n = 9$; median values indicated). The line shows the median, the box boundaries show the 25th and 75th percentiles, and the whiskers show the minimum and maximum values. One-tailed unpaired Student's *t*-test $^{*}P = 0.0316$ ($n = 8$ saline, $n = 9$ BoNT/A mice). **c**, Created in BioRender. S. Grelet (2025) https://biorender.com/mprd95w. **d**, Created in BioRender. S. Grelet (2025) https://biorender.com/98cu18d. **g**, Created in BioRender. S. Grelet (2025) https://biorender.com/xapzg43.

BoNT/A-denervated side of the prostate had a lower mitochondrial load than the saline-injected side, supporting the hypothesis that nerves promote mitochondrial load in cancer cells, with mitochondrial transfer as a contributing factor (Fig. 2c and Supplementary Tables 6 and 7).

Using a BALB/c mouse xenograft model, we evaluated mitochondrial transfer from mouse host neurons to 4T1 breast cancer cells in vivo (Fig. 2d). We designed a lentiviral construct encoding a neuron-specific, Syn1-GFP-OMP25, mitochondria-anchored eGFP reporter to label the mitochondria of host mammary fat pad neurons (Fig. 2e and Extended Data Fig. 5a–c). After genetic modification of the mouse DRG innervating the lower mammary fat pads, $4T1^{mCherry+}$ cancer cells were injected into the corresponding fat pads, and flow cytometry analysis of the primary cancer showed a subpopulation of cancer cells exhibiting the green signal of eGFP, consistent with mitochondrial transfer from mouse neurons to cancer cells in situ (Fig. 2e). We developed a similar lentiviral construct as a control, in which eGFP was targeted to the nucleus (GFP-NLS); this construct was non-transferable and showed no signal transfer between mouse nerves and $4T1^{mCherry+}$ cells (Fig. 2e).

We further assessed mitochondrial transfer by analysing mtDNA heteroplasmy arising from a mtDNA polymorphism identified between the mouse host and cancer cells, as identified by Sanger sequencing (Fig. 2f), with this analysis serving as an additional independent approach. $4T1^{mCherry+}$ cells from cancer xenografts were FACS-sorted

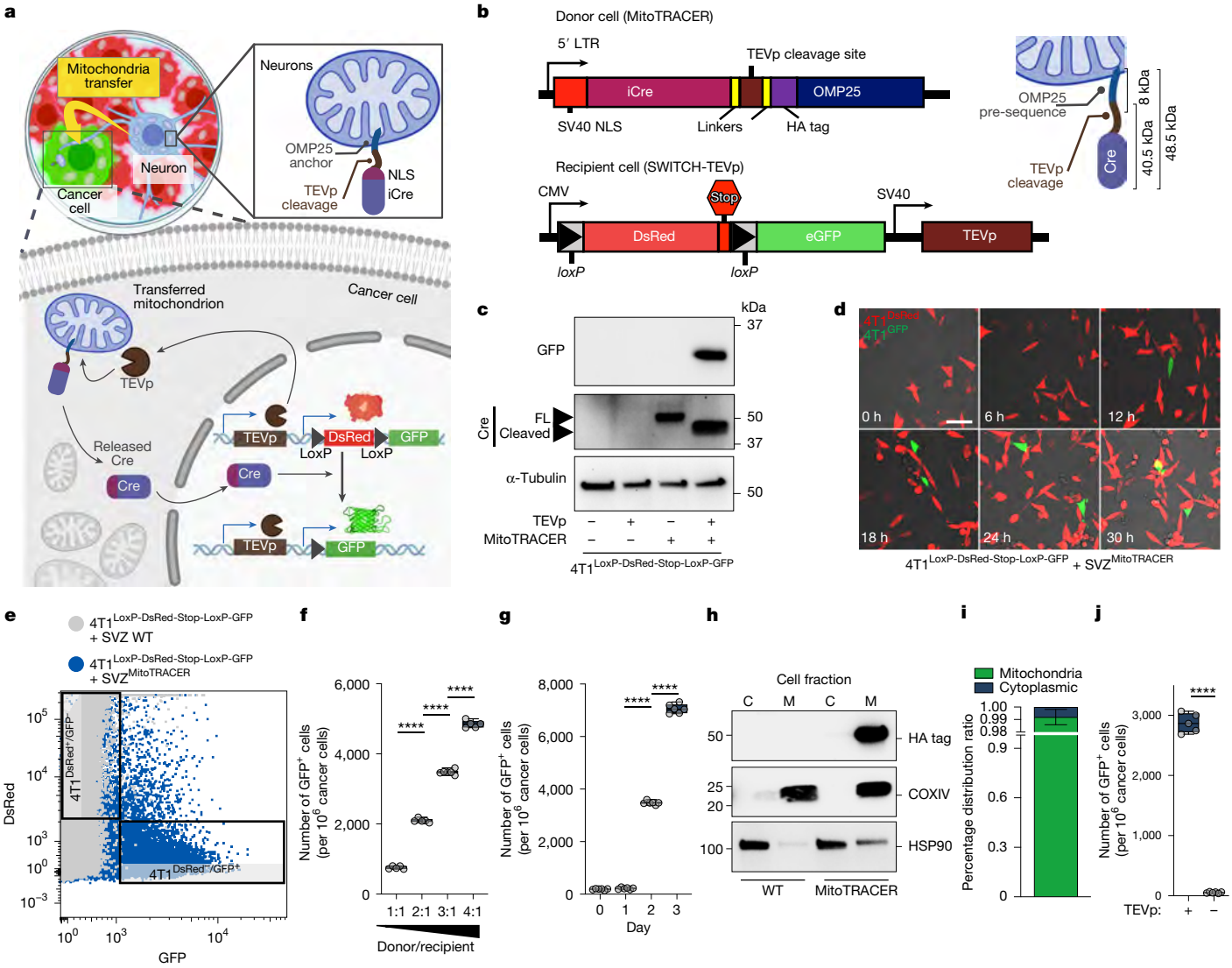

Fig. 3 | MitoTRACER for lineage tracing of cell–cell transfer of mitochondria. **a**,**b**, MitoTRACER strategy. Donor neurons express mitochondria-targeted Cre recombinase (iCre) with an SV40 nuclear localization signal (NLS-iCre), linked to the OMP25 mitochondrial outer membrane domain. Recipient cells express both a loxP-DsRed-Express2-Stop-loxP-eGFP switch and the TEVp. After transfer, TEVp cleaves NLS-iCre, enabling nuclear localization and excision of DsRed-Express2, resulting in a permanent change from DsRed (red) to eGFP (green) expression. LTR, long terminal repeat. **c**, 4T1$^{\text{loxP-DsRed-Express2-Stop-loxP-eGFP}}$ co-expressing both MitoTRACER and TEVp shows efficient NLS-iCre cleavage and eGFP expression activation. No unintended cleavage was detected in the absence of TEVp expression. The same sample extracts were loaded in different gels. Representative experiment ($n = 3$). FL, full length. **d**,**e**, Confocal microscopy (**d**) and flow cytometry (**e**) of SVZ neuron–4T1 coculture confirmed red-to-green conversion, confirming the transfers and suitability of the approach for high-throughput analysis and collection of recipient cells. WT, wild type. Scale bar, 50 µm. **f**, Dose-dependent increase of mitochondrial transfer with donor-to-recipient ratios (1:1 to 4:1). The centre line shows the median, the box boundaries show the 25th and 75th percentiles, and the whiskers show the minimum and maximum values. Student's two-tailed unpaired *t*-test, $^{****}P < 0.0001$ ($n = 5$ independent cocultures). **g**, Time-dependent and cumulative increase of mitochondrial transfer from day 1 to day 3. The centre line shows the median, the box boundaries show the 25th and 75th percentiles, and the whiskers show the minimum and maximum values. Student's two-tailed unpaired *t*-test, $^{****}P < 0.0001$ ($n = 6$ independent cocultures). **h**,**i**, Western blot (**h**) and densitometry analysis (**i**) of the MitoTRACER subcellular localization through the HA tag expression on the construct confirmed its mitochondrial localization. Expression of COXIV and HSP90 validated the subcellular fraction purity. The same sample extracts were loaded in different gels. Representative experiment ($n = 3$) (mean ± s.d.; $n = 4$ independent experiments). C, cytoplasmic fraction; M, mitochondrial fraction. **j**, Coculture using recipient cells lacking TEVp confirmed the signal's specificity. The line shows the median, the box boundaries show the 25th–75th percentiles, and the whiskers show the minimum and maximum values. Student's two-tailed unpaired *t*-test, $P = 2.16463 \times 10^{-10}$, $^{****}P < 0.0001$ ($n = 5$ independent cocultures). **a**, Created in BioRender. S. Grelet (2025) https://biorender.com/aa3gfx0. **b**, Created in BioRender. S. Grelet (2025) https://biorender.com/ytn18rx.

and analysed for their mtDNA content through Nanopore sequencing, which confirmed the overall acquisition of mouse-derived mtDNA by cancer cells (Fig. 2g). The neuronal origin of these transfers was further validated through BoNT/A-mediated chemical denervation, which demonstrated that neurons accounted for approximately 35% of the total mitochondrial transfers between host neurons and cancer cells (Fig. 2g).

Permanent labelling of recipient cells

As the previous results established the biological relevance of nerve-to-cancer mitochondrial transfer in vitro and in vivo, and suggested its clinical relevance, it was important to investigate the effects of mitochondrial transfer on cancer cell biology. However, the ρ^0 4T1 cell model (Fig. 1l–q) was limited in biological relevance for studying the

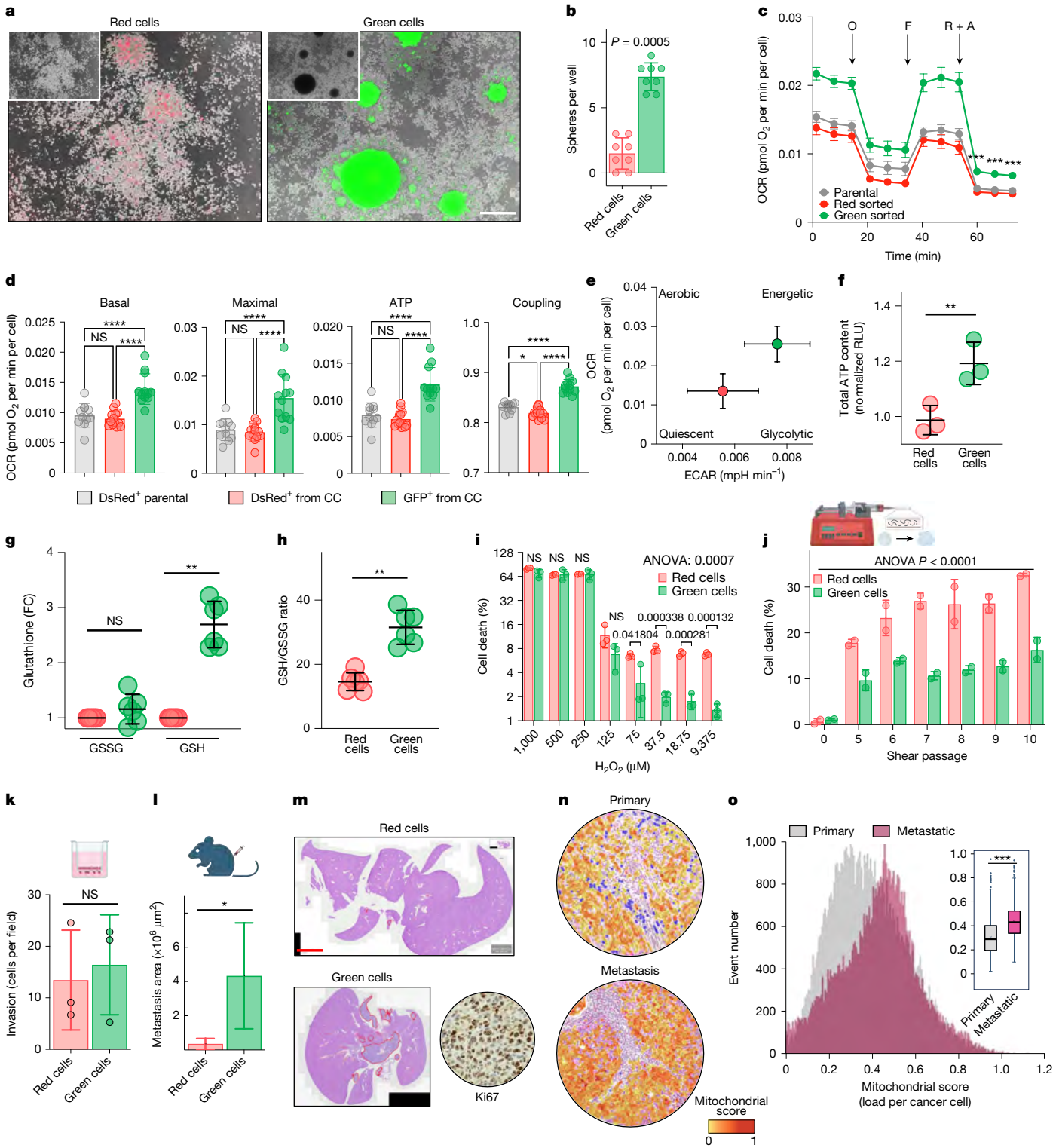

Fig. 4 | See next page for caption.

functional consequences of mitochondrial transfer in recipient cells. In addition, the mitochondrial-bound methods used in vitro (Fig. 1e–k) and in vivo (Fig. 2d,e) were limited to mitochondrial transfer at the time of analysis and could not evaluate previous transfers. Furthermore, after an eGFP-labelled mitochondrion entered a recipient cell, the eGFP signal faded quickly because the recipient cells did not express the mitochondrial genetic reporter. Therefore, these methods do not allow for distinguishing between cells in the same culture that received mitochondria versus those that did not, nor do they enable lineage tracing of recipient cells and their progeny. To address this limitation, we designed a new genetic reporter strategy known as MitoTRACER to permanently label the recipient cancer cells after mitochondrial transfer from neurons and distinguish them from cells that did not receive mitochondria.

In the MitoTRACER method, the recipient cells constitutively express a red (DsRed-Express2) fluorophore (hereafter referred to as red cells) until they receive mitochondria from the donor cells, which triggers the removal of the red fluorescence expression and activates the permanent expression of the eGFP green fluorophore

Fig. 4 | Neuron-to-cancer mitochondrial transfer enhances cancer OXPHOS, stemness and resistance to metastatic stressors. a, 4T1 recipient (green) cells sorted after MitoTRACER coculture showed spontaneous sphere formation capacities. Scale bar, 500 µm. **b**, Mammosphere formation assay confirmed increased stemness potential in green cells (***$P = 0.0005$, $n = 8$ independent cultures). Student's unpaired two-tailed *t*-test. **c**,**d**, Recipient green cells show enhanced mitochondrial OXPHOS capacities. CC, coculture. Representative profile ($n = 3$); mean ± s.e.m., parental: $n = 11$, red: $n = 13$, green: $n = 12$ cell cultures; Student's unpaired two-tailed *t*-test, *$P = 0.037$, ***$P < 0.001$, ****$P < 0.0001$. **e**, Energy map shows a more aerobic and energetic phenotype in green cells compared to the red counterpart (mean ± s.d. $n = 24$). ECAR, extracellular acidification rate. **f**, Luminescence-based assay of total cellular ATP content showed significantly higher levels in green cells (**$P = 0.0044$, $n = 3$ independent cultures). RLU, relative light units normalized per cell. Mean ± s.d., Student's two-tailed paired *t*-test. **g**,**h**, Green cells exhibited increased GSH (***$P = 0.0002$, $n = 6$ independent cultures) and overall improved GSH/GSSG ratios (**$P = 0.0028$ (**g**), **$P < 0.01$ (**h**), $n = 6$ independent cultures). Mean ± s.d., Student's two-tailed paired *t*-test. FC, fold change. **i**,**j**, Green cells exhibited higher tolerance to H_2O_2-induced oxidative stress (**i**; mean ± s.d., Student's two-tailed paired *t*-test, NS, not significant; two-way ANOVA, $P = 0.0007$) and greater resistance to shear stress (**j**; two-way ANOVA, $P < 0.001$). Representative profile ($n = 3$). **k**, Modified Boyden chamber assay revealed no change in intrinsic invasion capacity between green and red cells in vitro (NS, not significant; Student's two-tailed *t*-test, $n = 3$ independent cultures). **l**, In vivo, metastatic progression was enhanced in green versus red cells in mouse mammary fat pad xenografts, as observed by increased liver metastasis (mean ± s.d.; Student's two-tailed unpaired *t*-test, *$P = 0.01997$, $n = 8$ mice). **m**, Haematoxylin and eosin liver sections showed metastatic lesions, and Ki67 immunostaining confirmed the cancerous character of the lesions. Scale bar, 4 mm. **n**,**o**, Multispectral imaging in human breast cancer and matched metastatic sites revealed increased mitochondrial content at metastatic versus primary sites. Representative image from patient breast cancer samples (**n**) and matching metastasis and mitochondrial score quantification curve in the samples set (**o**). The line shows the median, the box boundaries show the 25th and 75th percentiles, and the whiskers show the minimum and maximum values (two-sided Welch's *t*-test, ***$P < 0.001$; $n = 8$ patients). **k**,**l**, Created in BioRender. S. Grelet (2025) https://biorender.com/35rzyib.

in these cells (hereafter referred to as green cells; Fig. 3a). In brief, the SVZ-NSC^{MitoTRACER} donor cells were genetically labelled with a mitochondrial-anchored Cre recombinase, and recipient 4T1 cancer cells were equipped with a loxP-DsRed-Express2-Stop-loxP-eGFP switch (Fig. 3b). The addition of a specific tobacco etch virus protease (TEVp) proteolytic cleavage site to the donor construct was required for the release of the mitochondria-bound Cre recombinase and its nuclear translocation into the recipient cells (Fig. 3c and Extended Data Fig. 6a). In the MitoTRACER coculture, following the transfer of nerve-derived mitochondria to the recipient cancer cell, the Cre recombinase triggers the red-to-green switch of the recipient cells, as observed by using time-lapse fluorescence microscopy and flow cytometry analyses of the nerve–cancer coculture (Fig. 3d,e). Time-lapse microscopy of the MitoTRACER coculture revealed the development of a green signal in recipient cells following the establishment of tunnelling nanotube connections, further supporting the role of these structures in mitochondrial transfer (Extended Data Fig. 6b and Supplementary Video 3). The use of various donor cell types, such as SVZ (Supplementary Video 4), mouse embryonic fibroblasts (Supplementary Video 5) and 3T3-L1 pre-adipocytes (Supplementary Video 6), demonstrated successful mitochondrial tracking through time-lapse imaging.

No unintended signal activation was observed in recipient cells until donor cells were introduced into the coculture. Dose–response (Fig. 3f) and time-course (Fig. 3g) analyses of the coculture demonstrated the sensitivity of the MitoTRACER approach in capturing the dynamics of mitochondrial transfer and its cumulative capability. Subcellular fractionation of MitoTRACER expression confirmed that nearly all of the construct is anchored to mitochondrial organelles (Fig. 3h,i). Finally, MitoTRACER coculture with recipient cells lacking TEV protease showed no signal, indicating that no unintended self-cleavage and further transfer through non-mitochondrial routes, such as secretory pathways, occurred (Fig. 3j). Together, these findings demonstrate the efficacy of this system in allowing real-time observation of mitochondrial transfer to recipient cells and its permanent nature, enabling lineage tracing of recipient cells.

Functional imprint on recipient cells

We used MitoTRACER to examine the biological impact of the nerve–cancer transfer of mitochondria in the recipient cancer cells. We also examined their fate during cancer progression, both in vitro and in vivo. From the MitoTRACER coculture, we FACS-isolated cells that have received mitochondria from the neurons (4T1^{MitoTRACERGreen}) and those that have not (4T1^{MitoTRACERRed}). Separate subcultures of the red versus green cells obtained from the MitoTRACER coculture revealed distinct growth patterns. Green cells having received mitochondria had a higher propensity for anchorage-independent growth patterns and exhibited the development of spheres throughout the culture (Fig. 4a). Anchorage-independent growth capacities of cancer cells are associated with their stemness potential and are usually tied to specific metabolic profiles driven by mitochondrial metabolism[33–35]. We confirmed the increased stemness of the recipient cancer cells by a mammosphere formation assay (Fig. 4b). Metabolic profiling of mitochondrial metabolism of the recipient cells indicated enhanced respiratory capacities of the green recipient cancer cells compared to red cells exposed to the neurons but not having received mitochondria and to parental 4T1 cells that were not exposed to neurons (Fig. 4c,d). Energetic mapping of the red versus green cells indicated a shift towards a more energetic status, corresponding to increases in both the oxygen consumption rate and the extracellular acidification rate (Fig. 4e), and this metabolic shift was associated with a significant increase in basal and maximal respiration capacities of the cancer cells, increased coupling and increased ATP production (Fig. 4d,f). Analysis of the functional outcomes of mitochondrial transfer revealed improved redox balance in the recipient (green) cancer cells, as indicated by their higher levels of reduced glutathione (GSH) (Fig. 4g). This increase translated into an improved GSH to oxidized glutathione (GSSG) ratio (Fig. 4h), a key marker of cellular redox status[36]. We next confirmed that enhanced redox balance was associated with an increased capacity of recipient cancer cells to withstand oxidative stress (Fig. 4i) at physiological doses (9–75 µM) and greater resistance to shear stress (Fig. 4j).

Together, metabolic plasticity, improved redox balance and increased oxidative and shear stress resistance are hallmarks of metastatic cancer cells[37–39]. We therefore investigated whether mitochondrial transfer could enhance metastatic behaviours in cancer cells. In vitro analysis of the recipient cancer cells' invasive potential revealed no increase in intrinsic invasiveness (Fig. 4k). However, in vivo xenografts with recipient cells demonstrated significantly higher metastatic potential than their 'non-recipient' counterparts (Fig. 4l,m), suggesting that mitochondrial transfer may contribute to the metastatic cascade beyond the invasion process.

Pathological analysis of human breast cancer samples further underscored the role of mitochondria in tumour dissemination, with metastatic cells exhibiting a significant increase in mitochondrial load (Fig. 4n,o and Supplementary Tables 8 and 9). Together, our findings clearly suggest that mitochondrial transfer from neurons to cancer cells may enhance metastatic behaviour by strengthening the resilience of cells against metastatic stressors, such as oxidative and shear

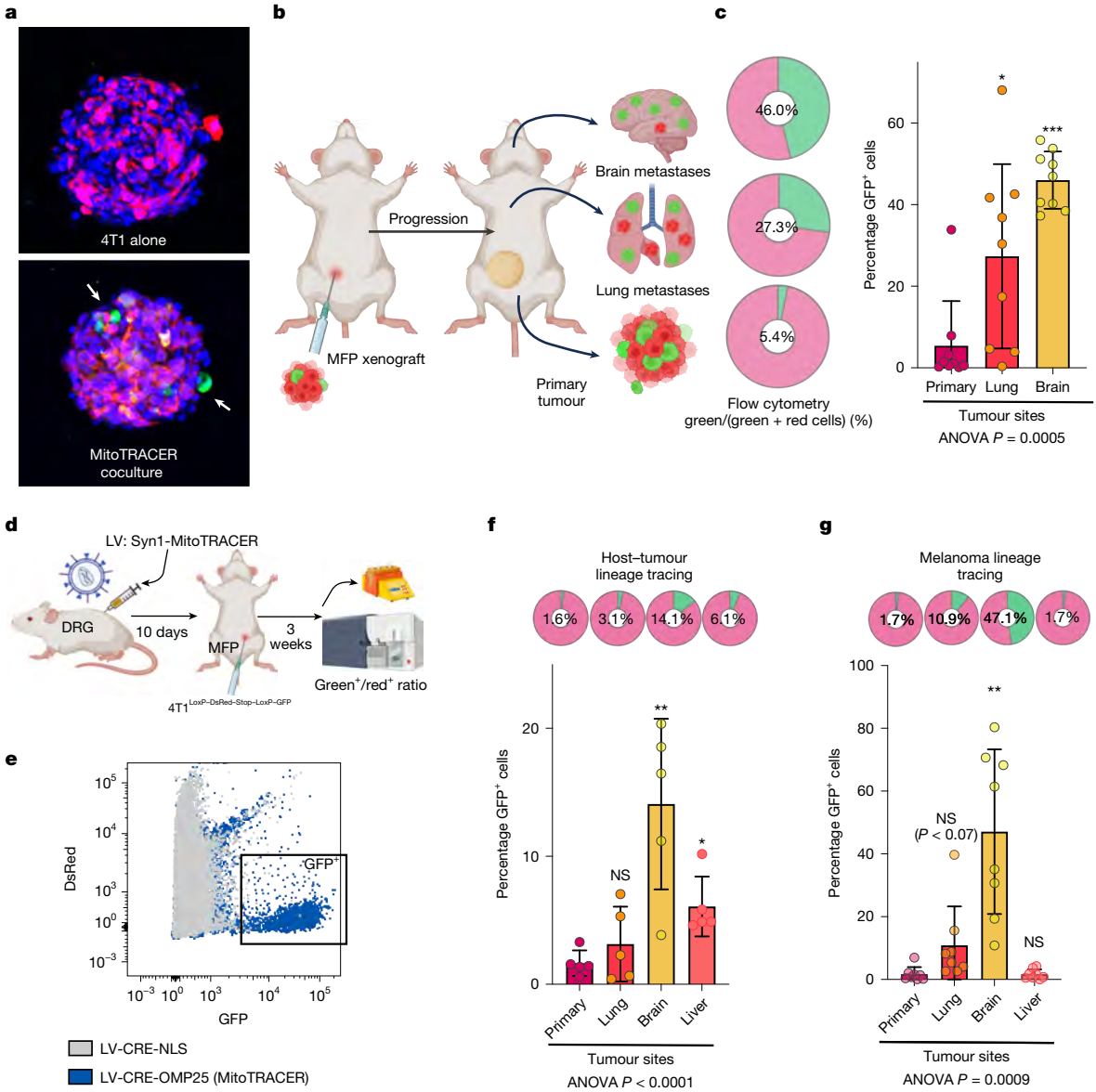

Fig. 5 | Lineage tracing of the intercellular transfer of mitochondria from neuron to cancer cell during breast cancer dissemination in vivo. a, 3D spheroids of SVZ-NSCs^{MitoTRACER} mixed with 4T1 recipient cancer cells confirmed mitochondria transfer, evidenced by red-to-green fluorescence conversion in 4T1 cells (white arrows). **b**,**c**, MitoTRACER spheroids were transplanted into mammary fat pads of BALB/c mice (**b**); after cancer progression, flow cytometry of cells isolated from primary tumours, lungs and brains revealed selective enrichment of green fluorescent cells (eGFP$^+$) in lung and brain metastases compared to the primary tumour (**c**). Mean ± s.d.; Student's two-tailed paired *t*-test, lung: $^*P = 0.018$, brain: $^{***}P = 1.2275 \times 10^{-6}$; $n = 9$ mice; ANOVA, $P = 0.0005$. **d**, Schematic of the procedure for lineage tracing of mitochondrial transfer between mouse host mammary neurons and cancer cells in vivo. Lentivirus expressing Syn1-MitoTRACER construct was injected into the DRG area, innervating the lower mammary fat pads. After 10 days, the SWITCH-TEVp-expressing 4T1 recipient cells were injected. Following tumour growth, tissues (primary, lung, brain and liver) were analysed for mitochondrial transfer by flow cytometry. **e**, Flow cytometry of primary tumours showed eGFP$^+$ cells, confirming mitochondrial transfer. Control lentivirus expressing Syn1-driven nuclear-localized Cre (LV-CRE-NLS) showed no green signal, validating the specificity of our approach. **f**, Ex vivo quantification of mitochondrial transfer in the primary tumour and lineage tracing of metastatic development in the lung, brain and liver showed significant enrichment of eGFP$^+$ cells in metastatic sites compared to the primary tumour (ANOVA, $P < 0.0001$), with significant enrichment in brain and liver metastases (mean ± s.d., Student's one-tailed paired *t*-test values, brain: $^{**}P = 0.0096$, liver: $^*P = 0.0215$; $n = 5$ mice). Top panel shows distribution of red and green cells. **g**, Validation using syngeneic B16-F1 melanoma cells co-injected with SVZ-NSCs^{MitoTRACER} as mixed-cell spheroids in C57BL/6 mice showed significant mitochondrial transfer enrichment in brain metastases (mean ± s.d., ANOVA, $P = 0.0009$; Student's one-tailed paired *t*-test, brain: $^{**}P = 0.0017$; $n = 8$ mice). Top panel shows distribution of red and green cells. **b**, Created in BioRender. S. Grelet (2025) https://biorender.com/culfgzj. **d**, Created in BioRender. S. Grelet (2025) https://biorender.com/2w7o7rr.

stress, thereby augmenting their metastatic potential through adaptive mechanisms.

Recipient cell fate during metastasis

The observed differences in mitochondrial load between primary and metastatic cancer suggested that mitochondria-recipient cancer cells in primary tumours may possess enhanced metastatic potential. The metastatic cascade is inefficient, with cancer cells encountering multiple stressors that impede their successful dissemination and growth at secondary sites[40]. Metabolic reprogramming and plasticity have emerged as crucial adaptive mechanisms for the successful metastatic dissemination of cancer cells[5,41–43]. Thus, we reasoned that neuron-derived mitochondria confer enhanced metabolic adaptability

and resilience, enabling recipient cancer cells to better spread and ultimately survive and proliferate at distant sites. To test this hypothesis, we performed lineage tracing to follow the fate of primary cancer cells receiving mitochondria from nerves.

We developed a preclinical model of the nerve–cancer transfer of mitochondria (Fig. 5). We combined the MitoTRACER coculture approach with the 4T1 mammary fat pad xenograft model that can fully recapitulate the breast cancer progression steps and metastasis of TNBC[44,45]. Mixed-cell spheroids of the MitoTRACER coculture (Fig. 5a) were transplanted into mammary fat pads. When the xenograft reached appropriate size, cancer cells were collected from the primary tumour and both lung and brain tissues, which are prevalent metastatic sites in TNBC. The cells were then analysed by flow cytometry to probe the ratio between $4T1^{Red+}$ versus $4T1^{Green+}$ cells (Fig. 5b). We observed the development of an average of about 5.4% $4T1^{GFP+}$ cells within the primary tumour. This proportion was significantly enriched in both lung and brain tissues to reach 27.3% and 46.0% of the total cancer cells in those sites, respectively (Fig. 5c). This demonstrates that cells that acquired mitochondria from the SVZ-NSCs within the primary tumour, or their progeny, are more likely to form distant metastases successfully. To extend the observations with implanted mixed-cell spheroids to a model of host-mediated neuronal mitochondrial transfer, we genetically modified mouse DRG in vivo using a lentivirus encoding a MitoTRACER construct driven by the synaptin1 promoter (LV-CRE-OMP25) or its non-transferable, nuclear-targeted variant (LV-CRE-NLS; Fig. 5d). At 10 days after lentiviral transduction, SWITCH-TEVp-expressing recipient cells were injected into the mammary fat pad, and tumours were subsequently excised to assess eGFP fluorophore expression, indicative of mouse-derived neuronal mitochondrial transfer into cancer cells (Fig. 5e). We observed only 1.6% $eGFP^+$ cells in the primary tumour, which was less than the 5.4% observed with the mixed-cell spheroids, probably owing to the lower nerve density in the tumour in situ, when compared to the spheroid model. Lineage tracing reproduced by labelling the endogenous nerve of the house mouse using lentiviruses injected into the DRG area also demonstrated a marked enrichment of $eGFP^+$ recipient cells in metastatic sites, with significant increases in the brain and liver compared to the primary tumour (Fig. 5f).

We tested whether nerve-mediated mitochondrial transfer may affect distant metastasis in another cancer progression model using the B16-F10 melanoma xenograft. The observations about transferred mitochondria in primary and metastatic tumours were similar in the melanoma and breast cancer models, but the rate of mitochondrial transfer was lower in the melanoma than in the 4T1 breast cancer model. Furthermore, the melanoma model showed no significant enrichment of green $eGFP^+$ cells in the lungs or liver but marked enrichment in the brain, corroborating findings from the breast cancer model and providing evidence that neuronal mitochondrial transfer may promote brain metastases with various cancer types (Fig. 5g).

Discussion

The nerve–cancer interplay was initially discovered in prostate cancer, in which cancer cells can promote cancer innervation by expressing axon guidance molecules, such as semaphorins, promoting neuronal progenitor differentiation in the cancer stroma and the establishment of the nerve–cancer interface[17,46–48]. Initial observations in prostate cancer have shown how the aberrant expression of semaphorin 4F by cancer cells promotes increased prostate nerve density and cancer aggressiveness[18,49]. Later studies supported the relevance of semaphorin 4F in other biological contexts such as gastric cancer[19] and breast cancer[17], in which cancer cell plasticity triggers the expression of semaphorin 4F to promote cancer innervation and metastasis[50]. Our previous studies demonstrated how cancer innervation and cancer cell plasticity are intimately linked[17,50], and although progress has been made in understanding the mechanisms leading to cancer-mediated neuronal differentiation and the establishment of the nerve–cancer interface, the mechanisms and functional effects of neurons on breast cancer progression and metastatic potential remain incompletely understood. Our study demonstrates how cancer-induced neuron differentiation leads to marked neuronal metabolic reprogramming with clear functional consequences. We show that cancer-associated neurons are a significant source of mitochondria transferred to the cancer cell to induce their metabolic reprogramming and increase stemness potential.

Pathological analysis and animal denervation models, including the breast carcinoma denervation model presented herein, have consistently associated cancer nerve density with cancer invasion and metastasis[51–54]. Metabolic plasticity and stemness potential are essential hallmarks of cancer metastasis[55]. To test whether the nerve–cancer transfers of mitochondria relate to the development of distant metastasis, we developed the MitoTRACER genetic reporter capable of permanently marking recipient cells. We used this approach to create a preclinical model of nerve–cancer transfer of mitochondria in vivo. The fate mapping experiment revealed enrichment of mitochondria-recipient cancer cells or their progeny at metastatic tumour sites relative to the primary tumour, reflecting their increased capacities to achieve the metastatic colonization steps successfully. Although the exact molecular mechanisms remain unclear, our study shows that cancer cells acquiring mitochondria from neurons gain adaptive advantages, enabling resilience against metastatic stressors such as oxidative[39] and shear stress[37,38,56], which are well-known key barriers to metastasis. From a probabilistic point of view, cancer cells that energetically outperform others have a greater probability of moving and seeding. It is probably a selection process by which the incorporation of these neuronal mitochondria into the cancer cells provides an increased capacity to survive the metastatic process.

We noted selective enrichment of mitochondria-recipient cancer cells in brain metastases in both breast cancer and melanoma models. This suggests that mitochondrial acquisition from neurons may prime cancer cells to adapt more effectively to the brain's unique microenvironment. Previous research supports this idea, as brain-metastatic cancer cells must metabolically adapt to survive in the brain's nutrient-poor environment[57] due to the high energy demands of neurons[58].

Neuronal mitochondria are renowned for their highly efficient metabolic potential, which contributes to the superior metabolic efficiency of neurons compared to epithelial cells[59]. Therefore, cancer cell acquisition of neuron-derived mitochondria may provide them with an adequate metabolic arsenal to survive and successfully proliferate in the brain environment. Our findings also suggest that neurons may be particularly effective donors of mitochondria, probably owing to their abundant mitochondrial content and the establishment of strong contacts at the nerve–cancer interface. Further studies are needed to clarify whether the impact of neuronal mitochondria is primarily due to their intrinsic metabolic efficiency or simply their highest transfer frequency.

Collectively, our findings provide a compelling metabolic explanation for the observed dependency between cancer cells and nerves, potentially extending to broader contexts. These results advocate for more in-depth studies into underlying mechanisms and therapeutic strategies targeting nerve–cancer mitochondrial transfers to prevent metastatic disease.

Online content

Any methods, additional references, Nature Portfolio reporting summaries, source data, extended data, supplementary information, acknowledgements, peer review information; details of author contributions and competing interests; and statements of data and code availability are available at https://doi.org/10.1038/s41586-025-09176-8.

1. Ayala, G. Neuroepithelial interactions in cancer. *Annu. Rev. of Pathol.* **18**, 493–514 (2023).
2. Coarfa, C. et al. Influence of the neural microenvironment on prostate cancer. *Prostate* **78**, 128–139 (2018).
3. Magnon, C. & Hondermarck, H. The neural addiction of cancer. *Nat. Rev. Cancer* **23**, 317–334 (2023).
4. Torborg, S. R., Li, Z., Chan, J. E. & Tammela, T. Cellular and molecular mechanisms of plasticity in cancer. *Trends Cancer* **8**, 735–746 (2022).
5. Faubert, B., Solmonson, A. & DeBerardinis, R. J. Metabolic reprogramming and cancer progression. *Science* **368**, eaaw5473 (2020).
6. Mosier, J. A., Schwager, S. C., Boyajian, D. A. & Reinhart-King, C. A. Cancer cell metabolic plasticity in migration and metastasis. *Clin. Exp. Metastasis* **38**, 343–359 (2021).
7. DeBerardinis, R. J. & Chandel, N. S. Fundamentals of cancer metabolism. *Sci. Adv.* **2**, e1600200 (2016).
8. Xing, Y., Zhao, S., Zhou, B. P. & Mi, J. Metabolic reprogramming of the tumour microenvironment. *FEBS J.* **282**, 3892–3898 (2015).
9. Silverman, D. A. et al. Cancer-associated neurogenesis and nerve-cancer crosstalk. *Cancer Res.* **81**, 1431–1440 (2020).
10. Reavis, H. D., Chen, H. I. & Drapkin, R. Tumor innervation: cancer has some nerve. *Trends Cancer* **6**, 1059–1067 (2020).
11. Ali, S. R., Jordan, M., Nagarajan, P. & Amit, M. Nerve density and neuronal biomarkers in cancer. *Cancers* **14**, 4817 (2022).
12. Li, D. et al. High nerve density in breast cancer is associated with poor patient outcome. *FASEB Bioadv.* **4**, 391–401 (2022).
13. Liebig, C., Ayala, G., Wilks, J. A., Berger, D. H. & Albo, D. Perineural invasion in cancer. *Cancer* **115**, 3379–3391 (2009).
14. Mauffrey, P. et al. Progenitors from the central nervous system drive neurogenesis in cancer. *Nature* **569**, 672–678 (2019).
15. Kappos, E. A. et al. Denervation leads to volume regression in breast cancer. *J. Plast. Reconstr. Aesthet. Surg.* **71**, 833–839 (2018).
16. Behbod, F. et al. An intraductal human-in-mouse transplantation model mimics the subtypes of ductal carcinoma in situ. *Breast Cancer Res.* **11**, R66 (2009).
17. Grelet, S. et al. TGFβ-induced expression of long noncoding lincRNA Platr18 controls breast cancer axonogenesis. *Life Sci. Alliance* **5**, e202101261 (2022).
18. Ding, Y. et al. Semaphorin 4F as a critical regulator of neuroepithelial interactions and a biomarker of aggressive prostate cancer. *Clin. Cancer Res.* **19**, 6101–6111 (2013).
19. Wang, H. et al. Semaphorin4F is a potential biomarker for clinical progression and prognosis in gastric cancer. *Int. J. Clin. Exp. Pathol.* **16**, 210–224 (2023).
20. Agostini, M. et al. Metabolic reprogramming during neuronal differentiation. *Cell Death Differ.* **23**, 1502–1514 (2016).
21. Zheng, X. et al. Metabolic reprogramming during neuronal differentiation from aerobic glycolysis to neuronal oxidative phosphorylation. *eLife* **5**, e13374 (2016).
22. Borcherding, N. & Brestoff, J. R. The power and potential of mitochondria transfer. *Nature* **623**, 283–291 (2023).
23. Nakai, R. et al. Mitochondria transfer-based therapies reduce the morbidity and mortality of Leigh syndrome. *Nat. Metab.* **6**, 1886–1896 (2024).
24. Brestoff, J. R. et al. Intercellular mitochondria transfer to macrophages regulates white adipose tissue homeostasis and is impaired in obesity. *Cell Metab.* **33**, 270–282 (2021).
25. Kidwell, C. U. et al. Transferred mitochondria accumulate reactive oxygen species, promoting proliferation. *Elife* **12**, e85494 (2023).
26. Goliwas, K. F. et al. Mitochondrial transfer from cancer-associated fibroblasts increases migration in aggressive breast cancer. *J. Cell Sci.* **136**, jcs260419 (2023).
27. Watson, D. C. et al. GAP43-dependent mitochondria transfer from astrocytes enhances glioblastoma tumorigenicity. *Nat. Cancer* **4**, 648–664 (2023).
28. Khozhukhar, N., Spadafora, D., Rodriguez, Y. & Alexeyev, M. Elimination of mitochondrial DNA from mammalian cells. *Curr. Protoc. Cell Biol.* **78**, 20.11.1–20.11.14 (2018).
29. Kujoth, G. C. et al. Mitochondrial DNA mutations, oxidative stress, and apoptosis in mammalian aging. *Science* **309**, 481–484 (2005).
30. King, M. P. & Attardi, G. Human cells lacking mtDNA: repopulation with exogenous mitochondria by complementation. *Science* **246**, 500–503 (1989).
31. Spees, J. L., Olson, S. D., Whitney, M. J. & Prockop, D. J. Mitochondrial transfer between cells can rescue aerobic respiration. *Proc. Natl Acad. Sci. USA* **103**, 1283–1288 (2006).
32. Ruder, S. et al. Development and validation of a quantitative reactive stroma biomarker (qRS) for prostate cancer prognosis. *Hum. Pathol.* **122**, 84–91 (2022).
33. Sancho, P., Barneda, D. & Heeschen, C. Hallmarks of cancer stem cell metabolism. *Br. J. Cancer* **114**, 1305–1312 (2016).
34. Schafer, Z. T. et al. Antioxidant and oncogene rescue of metabolic defects caused by loss of matrix attachment. *Nature* **461**, 109–113 (2009).
35. Fiorillo, M., Sotgia, F. & Lisanti, M. P. "Energetic" cancer stem cells (e-CSCs): a new hyper-metabolic and proliferative tumor cell phenotype, driven by mitochondrial energy. *Front. Oncol.* **8**, 677 (2019).
36. Migaud, M. E., Ziegler, M. & Baur, J. A. Regulation of and challenges in targeting NAD^+ metabolism. *Nat. Rev. Mol. Cell Biol.* **25**, 822–840 (2024).
37. Huang, Q. et al. Fluid shear stress and tumor metastasis. *Am. J. Cancer Res.* **8**, 763–777 (2018).
38. Barnes, J. M., Nauseef, J. T. & Henry, M. D. Resistance to fluid shear stress is a conserved biophysical property of malignant cells. *PLoS ONE* **7**, e50973 (2012).
39. Piskounova, E. et al. Oxidative stress inhibits distant metastasis by human melanoma cells. *Nature* **527**, 186–191 (2015).
40. Dongre, A. & Weinberg, R. A. New insights into the mechanisms of epithelial-mesenchymal transition and implications for cancer. *Nat. Rev. Mol. Cell Biol.* **20**, 69–84 (2019).
41. Lehuédé, C., Dupuy, F., Rabinovitch, R., Jones, R. G. & Siegel, P. M. Metabolic plasticity as a determinant of tumor growth and metastasis. *Cancer Res.* **76**, 5201–5208 (2016).
42. Faubert, B. & DeBerardinis, R. J. Analyzing tumor metabolism in vivo. *Annu. Rev. Cancer Biol.* **1**, 99–117 (2017).
43. Valastyan, S. & Weinberg, R. A. Tumor metastasis: molecular insights and evolving paradigms. *Cell* **147**, 275–292 (2011).
44. Bailey-Downs, L. C. et al. Development and characterization of a preclinical model of breast cancer lung micrometastatic to macrometastatic progression. *PLoS ONE* **9**, e98624 (2014).
45. Yang, J. et al. Twist, a master regulator of morphogenesis, plays an essential role in tumor metastasis. *Cell* **117**, 927–939 (2004).
46. Ayala, G. E. et al. Cancer-related axonogenesis and neurogenesis in prostate cancer. *Clin. Cancer Res.* **14**, 7593–7603 (2008).
47. Allen, J. K. et al. Sustained adrenergic signaling promotes intratumoral innervation through BDNF induction. *Cancer Res.* **78**, 3233–3242 (2018).
48. Jurcak, N. R. et al. Axon guidance molecules promote perineural invasion and metastasis of orthotopic pancreatic tumors in mice. *Gastroenterology* **157**, 838–850 (2019).
49. Ayala, G. E. et al. In vitro dorsal root ganglia and human prostate cell line interaction: redefining perineural invasion in prostate cancer. *Prostate* **49**, 213–223 (2001).
50. Galappaththi, S. L., Katz, B., Howze, P. H., Hoover, G. & Grelet, S. A CRISPR/Cas9-based assay for high-throughput studies of cancer-induced innervation. *Cancers* **15**, 2026 (2023).
51. Magnon, C. et al. Autonomic nerve development contributes to prostate cancer progression. *Science* **341**, 1236361 (2013).
52. Shao, J. et al. Autonomic nervous infiltration positively correlates with pathological risk grading and poor prognosis in patients with lung adenocarcinoma. *Thorac. Cancer* **7**, 588–598 (2016).
53. Huang, D. et al. Nerve fibers in breast cancer tissues indicate aggressive tumor progression. *Medicine* **93**, e172 (2014).
54. Albo, D. et al. Neurogenesis in colorectal cancer is a marker of aggressive tumor behavior and poor outcomes. *Cancer* **117**, 4834–4845 (2011).
55. Krstic, J., Trivanovic, D., Jaukovic, A., Santibanez, J. F. & Bugarski, D. Metabolic plasticity of stem cells and macrophages in cancer. *Front. Immunol.* **8**, 939 (2017).
56. Ildiz, E. S., Gvozdenovic, A., Kovacs, W. J. & Aceto, N. Travelling under pressure - hypoxia and shear stress in the metastatic journey. *Clin. Exp. Metastasis* **40**, 375–394 (2023).
57. Fischer, G. M. et al. Molecular profiling reveals unique immune and metabolic features of melanoma brain metastases. *Cancer Discov.* **9**, 628–645 (2019).
58. Srinivasan, E. S., Deshpande, K., Neman, J., Winkler, F. & Khasraw, M. The microenvironment of brain metastases from solid tumors. *Neuro-oncol. Adv.* **3**, v121–v132 (2021).
59. Bray, N. Many makes of mitochondria. *Nat. Rev. Neurosci.* **20**, 645–645 (2019).

and S. Grelet assisted in the generation of ρ^0 cells; S. Grelet performed RNA-seq and Nanopore bioinformatics interpretation and wrote the code presented in the study; Y.D. and P.B. assisted in the processing and interpretation of pathology samples; J.T.C. designed and performed microarray bioinformatic and statistical gene-expression analyses in the Botox denervation model of ductal carcinoma in situ; F.B. and D.M. developed the intraductal breast carcinoma model; G.H., M.T.L., G.A. and S. Grelet performed and interpreted electrophysiology experiments and assisted in manuscript editing; and W.H. and T.W.P. assisted in experimental development and troubleshooting. S. Grelet wrote the manuscript, and S. Grelet and G.A. validated it. All authors reviewed the manuscript and approved the final version for publication.

Competing interests The MitoTRACER technology developed in this manuscript is covered under a pending patent application titled Methods and applications for monitoring mitochondrial transfer between donor and receiver cells, US Patent and Trademark Office, application number 18/885,864. S. Grelet and G.H. are listed as inventors of the technology.

Additional information

Supplementary information The online version contains supplementary material available at https://doi.org/10.1038/s41586-025-09176-8.

Correspondence and requests for materials should be addressed to Gustavo Ayala or Simon Grelet.

Peer review information *Nature* thanks Jonathan Brestoff, Yuan Pan and the other, anonymous, reviewer(s) for their contribution to the peer review of this work. Peer reviewer reports are available.